Steric hindrance effect of Schiff-base ligands on magnetic relaxation dynamics and emissive behavior of two dinuclear dysprosium complexes

Youdong Jiang, Sourav Dey, Hongshan Ke, Yongsheng Yang, Lin Sun, Gang Xie, Sanping Chen, Gopalan Rajaraman

PII: S1002-0721(22)00116-8

DOI: https://doi.org/10.1016/j.jre.2022.04.019

Reference: JRE 1211

To appear in: *Journal of Rare Earths*

Received Date: 22 February 2022

Revised Date: 12 April 2022

Accepted Date: 21 April 2022

Please cite this article as: Jiang Y, Dey S, Ke H, Yang Y, Sun L, Xie G, Chen S, Rajaraman G, Steric hindrance effect of Schiff-base ligands on magnetic relaxation dynamics and emissive behavior of two dinuclear dysprosium complexes, *Journal of Rare Earths*, https://doi.org/10.1016/j.jre.2022.04.019.

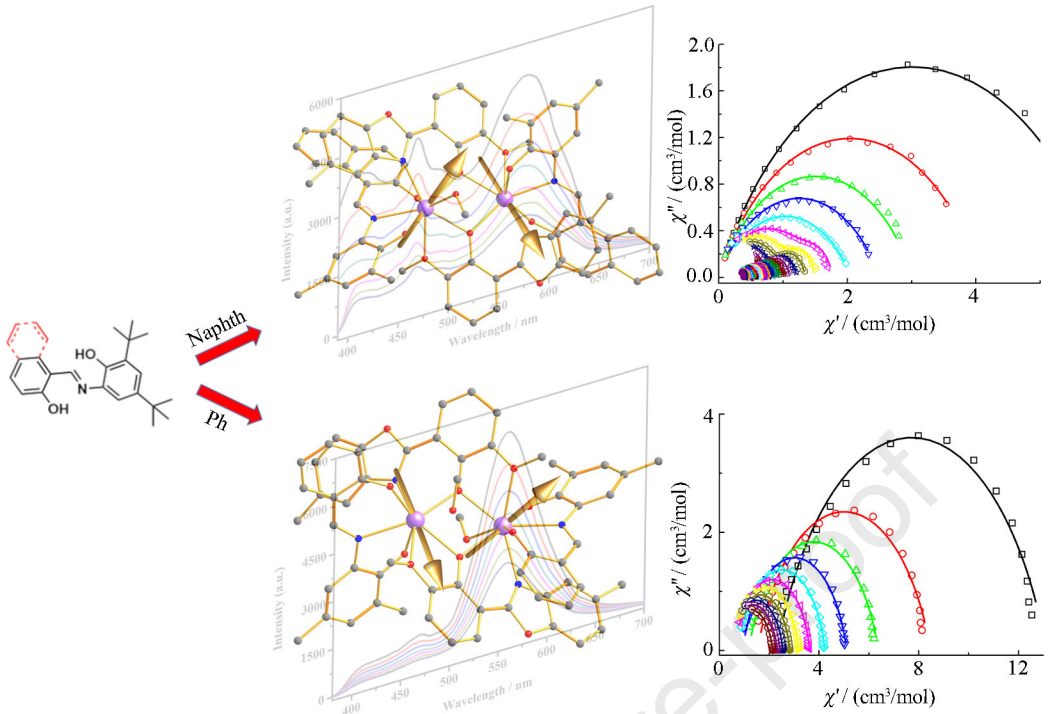

Steric hindrance effect of Schiff-base ligands on magnetic relaxation dynamics and emissive behavior of two dinuclear dysprosium complexes

Youdong Jiang,[a] Sourav Dey,[b] Hongshan Ke,[a, c*], Yongsheng Yang,[a] Lin Sun,[d] Gang Xie,[a] Sanping Chen,[a] Gopalan Rajaraman[b**]

[a]Key Laboratory of Synthetic and Natural Functional Molecule of the Ministry of Education, College of Chemistry and Materials Science, Northwest University, Xi'an 710127, China.

[b]Department of Chemistry, Indian Institute of Technology Bombay, Powai, Mumbai 400076, India.

[c]State Key Laboratory of Rare Earth Resource Utilization, Changchun Institute of Applied Chemistry, Chinese Academy of Sciences, Changchun 130022, China

[d]Henan Key Laboratory of Polyoxometalate Chemistry, Institute of Molecular and Crystal Engineering, College of Chemistry and Chemical Engineering, Henan University, Kaifeng 475004, China.

KEYWORDS: Fluorescent single-molecule magnets; Dinuclear dysprosium complexes; Mixed ligand; Steric hindrance; Theoretical calculations; Rare earths

ABSTRACT

The self-assembly reactions between mixed-ligand and tetrahydrate dysprosium acetate in the presence of mixed organic solvents led to two structural similar dinuclear dysprosium complexes with composition formulas of $Dy_2(L_1)_2(L_2)_2(CH_3OH)_2 \cdot CH_2Cl_2 \cdot CH_3OH$ (**1**) and $Dy_2(L_1)_2(L_3)_2(CH_3OH)_2 \cdot CH_3CN$ (**2**), where L_1, L_2 and L_3 represent the deprotonated form of 4-tert-butyl-2-(7-methoxybenzo[d]oxazol-2-yl)phenol, (E)-1-(((3,5-di-tert-butyl-2-hydroxyphenyl)imino)methyl)naphthalen-2-ol and (E)-2,4-di-tert-butyl-6-((2-hydroxybenzylidene)amino)phenol. The tiny difference of the core structure of **1** and **2** is derived from the steric hindrance of Schiff base ligand L_2 and L_3. Dynamic magnetic measurements reveal that **1** and **2** show frequency-dependent out-of-phase alternating-current susceptibility signal peaks at different

☆ **Foundation item**: Project supported by National Natural Science Foundation of China (21601143), Nature Science Foundation of Shaanxi Province (2021JM309), Open Funds of the State Key Laboratory of Rare Earth Resource of Changchun Institute of Applied Chemistry (RERU2021012), Science and Technology Innovation Team Program of Shaanxi Province (2022TD-32) and DST/SERB (CRG/2018/000430, DST/SJF/CSA03/2018-10; SB/SJF/2019-20/12).

* Corresponding author. Key Laboratory of Synthetic and Natural Functional Molecule of the Ministry of Education, College of Chemistry and Materials Science, Northwest University, Xi'an 710127, China.
** Corresponding author.
E-mail addresses: hske@nwu.edu.cn (H.S. Ke), rajaraman@chem.iitb.ac.in (G. Rajaraman). Tel(Fax): +86 029-81535026

temperatures under zero dc field, diagnostic of single-molecule magnet behavior. The experimental derived energy barrier to magnetization reversal for **1** and **2** are 108(1), 47(2) and 33(3) K. Ab initio CASSCF calculations performed on **1** and **2** suggest that the origin of the difference in magnetic properties originates from the variation in the single-ion anisotropy that arises due to minor structural variation. Further, the equation to calculate the effective energy barrier for Dy_2 proposed earlier was found to yield an excellent agreement to the experimental results. Solid state fluorescence measurements performed on **1** and **2** demonstrate that both exhibit two ligands centered components of fluorescent emissive, in addition, with different emitting colors and chromaticity coordinates. The discrepancy of fluorescence and single molecule magnet behavior showed by **1** and **2** can be attributed to the steric hindrance effect of Schiff base ligands.

1. Introduction

Single ion magnetic anisotropy and magnetic exchange interaction play an essential role in modulating the magnetization dynamics of dinuclear dysprosium single-molecule magnets. With regard to single ion magnetic anisotropy, several strategies were documented to fine tune it via modifying the coordination geometry[1] and crystal field[2] as well as magnetic anisotropic axis of individual dysprosium ions. For example, Yamashita et al. clarified that different magnetic relaxation processes displayed by three dinuclear dysprosium complexes, which sandwiched by phthalocyaninato triple decker, was ascribed to individual dysprosium site with different coordination geometry and the resulting ligand field parameters.[2] Dunbar et al. demonstrated that the identical organic bridging ligand with neutral and radical forms modified the relative spatial arrangement of the two dysprosium centers of dinuclear compounds and achieved tuning magnetic relaxation dynamics through redox switching.[3] Konar et al. reported that the different degree of terminal ligands binding away from the easy plane (g_x, g_y) affected the quantum tunneling of magnetization on single ion anisotropy and the overall magnetic relaxation dynamics.[4]

Concerning the construction of dinuclear dysprosium single-molecule magnets, numerous types of organic ligands were involved in including diketones,[5] endohedral fullerenes,[6] phosphine oxide derivatives,[7] carboxylates,[8] arylamidos,[9] Schiff-base,[10] cyclopentadienyls,[11] diazabutadiene,[12] phenolates,[13] hydroxyquinolines,[14] polyoxometalates,[15] phthalocyaninatos,[16] and amino-alcohols.[17] Moreover, the mixed-ligand strategy was also employed to prepare such complexes. The hybrid ligands consisted of diketones/Schiff-base,[18] tris(pyrazolyl) borate,[19] tetrathiafulvalene,[20] nitronyl nitroxide radical,[21] bipyrimidine-N-oxide,[22] hydroxylquinoline,[23] amino-alcohol,[24] pyrazolyl-tetrazine,[25] biphosphate,[26] and Schiff-base/calixarene,[27] dianthracene,[28] phthalocyanine,[29] and tris(pyrazolyl) borate/tetraoxolene,[30] cyclopentadienyl/radical,[31] as well as phthalocyanine/aldehyde,[2] and porphyrinato.[32] To our surprise, the mixed ligands containing Schiff-base and oxazole derivatives have been less explored. Recently, we reported the synergistic effect of such hybrid ligands on the anisotropy axis of two dinuclear dysprosium complexes.[33] Now we expand our investigation on the steric hindrance effect of Schiff base ligands on magnetic relaxation dynamics of dinuclear dysprosium complexes self-assembled from such mixed-ligand (Scheme S1).

Fluorescent single-molecule magnets hybrid-functional dysprosium-based complexes have attracted a great deal of attention in multidisciplinary areas. We are interested in the appropriate organic ligands employed to synthesize them. According to our literature survey, organic ligands including naphthalene diols,[34] (pyridylamino)phenol,[35] carboxylate acids,[36] rhodamine 6G,[37] rhodamine salicyladehyde hydrazone,[28] trizolate,[38] Schiff-base derivative,[39] quinolinol derivative and 1,10-phenanthroline,[40] anthracene group and hexafluoroacetylacetonate[41] have been reported previously. The examples of mixed-ligand[42–43] were rarely explored and deserve to be expanded in the exploration of fluorescent and single molecule magnetism bifunctional dysprosium systems.

Here we demonstrate the steric hindrance effect of Schiff base ligands on magnetic relaxation dynamics and emissive behavior of two dinuclear dysprosium complexes. Two structural similar dinuclear dysprosium complexes with composition formulas of $Dy_2(L_1)_2(L_2)_2(CH_3OH)_2 \cdot CH_2Cl_2 \cdot CH_3OH$ (**1**) and $Dy_2(L_1)_2(L_3)_2(CH_3OH)_2 \cdot CH_3CN$ (**2**), where L_1, L_2 and L_3 represent the deprotonated form of 4-tert-butyl-2-(7-methoxybenzo[d]oxazol-2-yl)phenol, (E)-1-(((3,5-di-tert-butyl-2-hydroxyphenyl)imino)methyl)naphthalen-2-ol and (E)-2,4-di-tert-butyl-6-((2-hydroxybenzylidene)amino)phenol, were characterized with the aid of solid-state X-ray single crystal structural analysis, magnetic properties measurements, fluorescent performance and theoretical calculations. The tiny difference of the core structure of **1** and **2** is derived from the steric hindrance of Schiff base ligand L_2 and L_3. Dynamic magnetic measurements reveal that **1** and **2** show frequency-dependent out-of-phase alternating-current susceptibility signal peaks at different temperatures under zero dc field, diagnostic of single-molecule magnet behavior. The experimental derived energy barrier to magnetization reversal for **1** and **2** are 108(1), 47(2) and 33(3) K, where the former displaying two magnetic relaxation processes at the intermediate temperatures. Quantum chemical calculations based on ab initio CASSCF/RASSI-SO/SINGLE_ANISO method were employed to disclose the reason behind the noticeable discrepancy of dynamic magnetization relaxation between **1** and **2**. Solid state fluorescence measurements performed on **1** and **2** demonstrate that both exhibit two ligands centered components of fluorescent emissive, in addition, with different emitting colors and chromaticity coordinates. The discrepancy of fluorescence and single molecule magnet behavior showed by **1** and **2** can be attributed to the steric hindrance effect of Schiff base ligands.

2. Experimental

2.1. Materials and synthesis

All reactions and manipulations were operated under aerobic conditions, using materials as received without further purification. $Dy(CH_3COO)_3 \cdot 4H_2O$ was acquired by dissolving dysprosium oxide in acetate acid. The synthesis of 2-amino-4,6-di-tert-butylphenol was accomplished by a method previously published in the literatures.[44–45]

2.2. Syntheses of HL_1, H_2L_2 and H_2L_3

The ligand 4-tert-butyl-2-(7-methoxybenzo[d]oxazol-2-yl)phenol (HL_1) was obtained according to a previous procedure reported by us.[33] The Schiff-base ligand (E)-1-(((3,5-di-tert-butyl-2-hydroxyphenyl)imino)methyl)naphthalen-2-ol (H_2L_2) was prepared by a condensation of 2-amino-4,6-

di-tert-butylphenol and 2-hydroxy-1-naphthaldehyde in a 1:1 molar ratio in ethanol.[33] The yellow solid product that formed was filtered, washed with cooled ethanol three times and dried under vacuum. Yield 6.76 g, 85%. ^{1}H NMR (400 MHz, d_6-DMSO, Fig. S1): δ 15.4 (d, 1H), 9.49 (d, 1H), 8.62 (s, 1H), 8.47 (d, 1H), 7.87 (d, 1H), 7.75 (d, 1H), 7.53 (t, 1H), 7.49 (d, 1H), 7.32 (t, 1H), 7.15 (d, 1H), 6.97 (d, 1H), 5.76 (s, 1H), 1.40 (s, 9H), 1.34 (s, 9H).

The procedure of synthesis of H_2L_3 was very similar to that of H_2L_2, using salicylaldehyde instead of 2-hydroxy-1-naphthaldehyde. The yellow needlelike product that formed was filtered, washed with cooled ethanol three times and dried under vacuum. Yield 5.53 g, 85%. ^{1}H NMR (400 MHz, d_6-DMSO, Fig. S2): δ 12.26 (s, 1H), 8.86 (s, 1H), 8.51 (s, 1H), 7.78 (d, 1H), 7.39 (t, 1H), 7.14 (d, 1H), 7.09 (d, 1H), 6.97 (d, 1H), 6.94 (d, 1H), 5.76 (s, 1H), 1.40 (s, 9H), 1.29 (s, 9H).

2.3. Syntheses of compounds **1** and **2**

$[Dy_2(L_1)_2(L_2)_2(CH_3OH)_2]\cdot CH_2Cl_2\cdot CH_3OH$ (**1**) A methanolic solution of triethylamine (0.20 mL, 0.20 mmol) was added to a mixture of H_2L_2 (18.8 mg, 0.05 mmol) and HL_1 (14.9 mg, 0.05 mmol) in 10 mL of methanol under continuous stirring. After 40 min, solid $Dy(CH_3COO)_3\cdot 4H_2O$ (18 mg, 0.05 mmol) was added to the above mixture and stirred continuously for 3 h. 10 mL of dichloromethane was subsequently added to the reaction mixture and stirred for 15 min before filtering. The filtrate was left undisturbed. Orange red block single crystals suitable for single-crystal structure determination were obtained after 3 d by slow evaporation of the solvent at room temperature. Yield 30 mg (65%, based on the ligand). IR (KBr pellet, cm^{-1}): 3432(w), 2595(s), 1606(s), 1539(s), 1466(s), 1369(w), 1338(w), 1243(m), 1207(m), 1148(w), 1080(w), 1036(m), 963(w), 861(w), 834(w), 738(m), 660(w), 517(w), 437(w). Elemental analysis calcd (%) for $Dy_2C_{90}H_{104}O_{13}N_4Cl_2$ (Mr = 1845.67): C, 58.57; H, 5.68; N, 3.04. Found: C, 58.38; H, 5.75; N, 3.01.

$[Dy_2(L_1)_2(L_3)_2(CH_3OH)_2]\cdot CH_3CN$ (**2**) The procedure for the synthesis of **2** was followed a similar way to that of **1**, using H_2L_3 and acetonitrile to substitute H_2L_2 and dichloromethane. Yellow plate single crystals suitable for single-crystal X-ray diffraction structure determination were obtained after one week by slow evaporation of the solvent at room temperature. Yield 17 mg (40%, based on the ligand). IR (KBr pellet, cm^{-1}): 3433(s), 3060(w), 2952(s), 1605(s), 1542(s), 1454(s), 1383(w), 1277(w), 1230(s), 1211(m), 1177(m), 1084(m), 1034(s), 941(w), 858(w), 832(m), 740(s), 664(w), 543(w), 458(w). Elemental analysis calcd (%) for $Dy_2C_{82}H_{97}O_{12}N_5$ (Mr = 1669.64): C, 58.99; H, 5.86; N, 4.19. Found: C, 58.60; H, 5.99; N, 4.09.

2.4. Physical measurements

Elemental analysis for C, H, and N was performed by a VarioEL element analyzer. A VERTEX 70 Fourier transform infrared (FTIR) spectrophotometer was used to record the FTIR spectra of as-synthesized complexes with KBr pellets, using the reflectance technique (4000–400 cm^{-1}). ^{1}H NMR spectra were carried out with a Bruker DRX-400 equipment at 400 MHz at 25 °C using d_6-DMSO as the solvent. Powder X-ray diffraction (PXRD) patterns were obtained using a Rigaku RU200 diffractometer with Cu Kα radiation of λ = 0.15406 nm ran at 60 kV under the scan rate of 5(°)/min and a step size of 0.3° in 2θ. Thermogravimetric analysis (TGA) was finished with a heating rate of 10

ºC/min under constant nitrogen flow, rising from room temperature to 800 ºC. Magnetic tests were finished from 2 to 300 K, resort to a Quantum Design MPMS XL-7 SQUID magnetometer with a 7 T magnet. The diamagnetic correction of the two complexes was estimated using Pascal's constant, and the diamagnetic contribution of the sample holder was corrected with magnetic data. In the magnetization experiment, the temperature was set as 2−5 K and the magnetic field was set as 0−7 T. Alternating current susceptibility manipulation was performed to collect the in-phase and out-of-phase components of the susceptibility of **1** and **2** powders. The data were obtained by reducing the temperature from 35 to 2 K in the absence of an external dc magnetic field and an oscillating frequency of 3.5×10^{-4} T, and with frequencies between 1 and 1000 Hz for **1** and 1 to 1500 Hz for **2**, respectively. The solid-state fluorescence measurements were recorded on a Hitachi F-4500 fluorescence spectrophotometer. Emission spectra were measured by employing a neutral filter of 320 nm or 380 nm.

2.5. X-ray single-crystal structure determinations

Crystallographic data were collected at 170 K for **1** and 140 K for **2** on a Bruker D8 VENTURE single-crystal diffractometer with Mo Kα radiation (λ = 0.071073 nm). Raw data were integrated and corrected through the SAINT processing program. The crystal structures were solved by direct methods and refined on F^2 through the full-matrix least-squares using the SHELXTL 2014 program.[46] Non-hydrogen atoms were refined anisotropically. Hydrogen atom were introduced in idealized positions and refined as a fixed geometry on their parent atoms. Positional disorders for partial tert-butyl groups were treated with partial occupancies. A summary of crystallographic data and details of data refinement for **1** and **2** is listed in Table S1. Selected bond lengths (nm) and angles (°) of **1** and **2** are presented in Table S2. The supplementary crystallographic data for **1** and **2** are deposited at the CCDC as reference numbers 2106337 (**1**) and 2106338 (**2**).

3. Results and discussion

3.1 Syntheses and crystal structure description of **1** and **2**

The combination of HL_1 ligand and Schiff base ligand H_2L_2 or H_2L_3 with $Dy(CH_3COO)_3 \cdot 4H_2O$ and NEt_3 in a 1:1:1:4 molar ratio in mixed solvent led to the successful generation of two homometallic dinuclear dysprosium complexes **1** and **2**. The composition formulas of **1** and **2** are $Dy_2(L_1)_2(L_2)_2(CH_3OH)_2 \cdot CH_2Cl_2 \cdot CH_3OH$ and $Dy_2(L_1)_2(L_3)_2(CH_3OH)_2 \cdot CH_3CN$, respectively. Both **1** and **2** crystallize in a triclinic space group $P\bar{1}$ with Z = 2. Their solid-state single crystal X-ray diffraction structures are shown in Fig. 1. The asymmetric units of **1** and **2** comprise the whole molecule. Detailed crystallographic information of **1** and **2** are presented in Table S1.

Both Dy^{III} metal centers in each complex are octa-coordinate and their coordination constitutions comprise N_2O_6 donor atoms. The double connections between Dy1 and Dy2 in **1** and **2** are completed by two phenoxides derived from two L_1 ligands. The Dy–O–Dy values are 106.44(13)° and 103.82(13)° in **1** as well 106.96(10)° and 103.82(9)° in **2**. The average Dy–O bond parameters of Dy1 and Dy2 are 0.2365(2) and 0.2369(8) nm in **1** as well 0.2369(1) and 0.2355(5) nm in **2**. The longest Dy1–O distance corresponds to Dy1–O1 of 0.2599(4) in **1** and 0.2566(3) nm in **2**; the shortest Dy1–O to Dy1–O8 of

0.2173(3) in **1** and 0.2201(2) nm in **2**. For Dy2–O series, the longest and shortest lengths are Dy2-O12 of 0.2640(4) in **1** and 0.2567(3) nm in **2**, and Dy2–O9 of 0.2199(3) in **1** and 0.2189(3) nm in **2**. The Dy–N bond distances of Dy1 and Dy2 are 0.2470(4), 0.2463(4), 0.2565(4) and 0.2413(4) nm in **1** in addition 0.2513(3), 0.2478(3), 0.2525(3) and 0.2479(3) nm in **2**. Detailed information about the bond lengths of donor atoms coordinated to Dy^{III} centers in **1** and **2** are summarized in Table S2. The Dy1···Dy2 separation is 0.3713(1) and 0.3740(5) nm, respectively. The crystal packing of **1** and **2** demonstrate that no inter-molecular hydrogen bond or π-π interactions exist between the dinuclear units (Fig. S3). The shortest Dy1···Dy1 distance is 0.94849(5) and 0.88535(7) nm for **1** and **2**, respectively.

To check the phase purity of **1** and **2**, PXRD was conducted, which demonstrates that an excellent match between the experimental and simulated patterns can be observed (Fig. S4). The thermal stability of **1** and **2** were characterized by thermogravimetric (TG) measurement (Fig. S5). The calculated result of the coordination geometry of Dy1 and Dy2 in **1** and **2** is listed in Table S3.[47] The coordination polyhedron of Dy centers in **1** and **2** all belong to triangular dodecahedron (D_{2d}). The detailed triangular dodecahedron parameters for Dy1 are 1.025 and 0.998, and Dy2 are 0.908 and 0.737.

3.2 Magnetic properties

Static direct current magnetic susceptibility measurements for **1** and **2** were conducted on polycrystalline solid state sample in the 300–2 K temperature range under a 0.1 T applied magnetic field. The curves are shown in the $\chi_M T$ vs. T form (Fig. 2). At room temperature, the $\chi_M T$ values of **1** and **2** are 28.23 and 28.38 $cm^3 \cdot K/mol$, which are very close to the theoretical value of 28.34 $cm^3 \cdot K/mol$ expected for two uncoupled Dy^{III} ions with free ion approximation. Upon cooling, $\chi_M T$ product of **1** and **2** undergoes gradual decrease from room temperature to 25.99 and 26.20 $cm^3 \cdot K/mol$ at 50 K and then abrupt drop at lower temperatures to the minimum of 22.59 and 22.70 $cm^3 \cdot K/mol$ at 2 K. The initial smooth fall of $\chi_M T$ value for **1** and **2** is mainly ascribed to the thermal depopulation of m_J levels of Dy^{III} ion, which derives from the splitting of the $^6H_{15/2}$ ground state by ligand field effect. The lower temperature decrease behavior may result from the small intramolecular antiferromagnetic coupling interaction between Dy^{III} spin centers.

The field dependence of molar magnetization performed at 2, 3, and 5 K for **1** and **2** are presented in Fig. S6. Both plots undergo a steep increase at low fields up to 1 T and a slow rise at high fields up to 7 T. At the highest field, the magnetization values at different temperatures approach 12.50, 12.51, 12.47 μ_B in **1** and 11.20, 11.19, 11.18 μ_B in **2**. These maximums of magnetization are lower than the theoretical saturated value for two essentially isolated Dy^{III} ions of 20 μ_B with $J = 15/2$ and $g = 4/3$. In addition, magnetization versus applied direct-current field scan conducted on both complexes at 2 K display no hysteresis loop (Fig. S7).

We performed variable frequency alternating-current (ac) magnetic susceptibility measurements under zero direct-current field adopting an oscillating field of 3.5×10^{-4} T. The measured frequencies range between 1–1000 and 1–1500 Hz for **1** and **2**, respectively. The in-phase and out of phase components for **1** and **2** are depicted in Fig. S8 and Fig. 3. Both **1** and **2** display out-of-phase signal maxima accompanied by frequencies varied, indicating clear single-molecule magnets behavior character. Upon

increasing the temperature, the common feature of **1** and **2** is the decrease of the signal intensities accompanied by the signal maxima moved to higher frequencies. Surprisingly, in the intermediate temperatures range between 7 to 14 K, two signal maxima can be observed for **1** and further consolidated by the in phase versus out-of-phase (Fig. S9) plot. However, single magnetic relaxation process is evident except for the intermediate temperatures for **1** and **2** in the full temperatures range. We adopted the fitting equation comprising two magnetic relaxation pathways reported previously to simultaneously analyze the frequency dependence in-phase and out-of-phase magnetic susceptibility components for **1** in the intermediated temperatures.[48] At other temperatures, single magnetic relaxation process is nicely fitted by virtue of the generalized Debye model for **1** and **2** in the whole temperatures.[49] The fitting results for **1** and **2** were listed in Table S4. The values related to the distribution of relaxation times for **1** with two step magnetic relaxation are α_1 = 0.15–0.37 and α_2 = 0.07–0.15. The corresponding α values related to the singe magnetic relaxation are 0.03–0.40 and 0.13–0.25 for **1** and **2**. The α values of **1** are larger than that of **2** indicating the wider distribution of relaxation times and the propensity of multiple relaxation pathways.

The nature logarithm form of relaxation times extracted from the simultaneously fitting frequency dependence of in-phase and out-of-phase magnetic susceptibility components versus the inverse of the temperatures for **1** and **2** generates the plot in Fig. 4. It is obvious that the curve of **1** consists of two temperature range regions of 2–14 K and 7–31 K. For 7–31 K, Arrhenius equation in 16–31 K linear fitting yields the effective energy barrier for magnetization reversal of 108(1) K and pre-exponential factor of 5.86×10^{-6} s. The 7–31 K temperature domain was fitted taking Orbach and Raman relaxation processes into account (Eq. (1)). The fitting results in

$$\tau^{-1} = CT^{n} + {\tau_0}^{-1}\exp(-U_{\text{eff}}/k_{\text{B}}T) \quad (1)$$

C = 1.44 s^{-1} K^{-n}, n = 1.87, $\tau_0 = 3.93 \times 10^{-7}$ s, and U_{eff} = 186(3) K. For 2–14 K, Arrhenius law employed in 6–14 K generates energy barrier of 47(2) K and pre-exponential factor of 9.48×10^{-7} s. Combination of Orbach and QTM processes with Eq. (2) to evaluate the 2–14 K gives $\tau_{\text{QTM}} = 1.26 \times 10^{-2}$ s, U_{eff} = 45(2) K, and $\tau_0 = 1.17 \times 10^{-6}$ s. Again, for **2**,

$$\tau^{-1} = {\tau_{\text{QTM}}}^{-1} + {\tau_0}^{-1} \exp\left(-\frac{U_{\text{eff}}}{k_{\text{B}}T}\right) \quad (2)$$

Arrhenius equation in 6–12 K yields energy barrier of 33(3) K and pre-exponential factor of 7.8×10^{-6} s. Employing Eq. (2) to fit the entire temperature range results in $\tau_{\text{QTM}} = 5.54 \times 10^{-3}$ s, U_{eff} = 35(4) K, and $\tau_0 = 6.47 \times 10^{-6}$ s.

3.3 Fluorescence properties

We recorded the solid-state fluorescence spectra under excitation at 280–340 nm. As shown in Fig. S10, **1** and **2** display strong emission peaks at 578 and 560 nm, corresponding to the intra-ligand charge transfer emission from HL_1 ligand. Obviously, a weak broad emission in 400–475 nm region observed for **2** could be attributed to the Schiff base part of H_2L_3. However, at 470 nm vicinity relatively sharp intermediate emission peaks for **1** originates from the contribution of the Schiff base part of H_2L_2. The discrepancy of solid fluorescence properties below 470 nm range of **1** and **2** mainly results from the

difference of steric hindrances (naphthyl for H_2L_2 and phenyl for H_2L_3)[50] attached to the Schiff-base ligand, which further confirmed by the solid fluorescence measurement on the sole ligand (Fig. S11). At room temperature the calculated Commission Internationale del'Eclairage (CIE) chromaticity coordinate is (0.32, 0.35) for **1** upon excitation at 280 nm, which is close to the ideal white-light coordinates,[38] and (0.38, 0.50) for **2** upon excitation at 280 nm corresponding to the yellowish-green fluorescence.

3.4 Theoretical studies

Ab initio CASSCF/RASSI-SO/SINGLE_ANISO calculations were performed on the individual Dy(III) centres on complexes **1** and **2** using MOLCAS 8.4 programme package (see computational details for more information). The employed methodology is known to yield reasonable numerical estimates with the experimental results.[51] The calculation has been performed on the X-ray crystal structure by the diamagnetic substitution method by replacing one of the Dy centres with Lu (Fig. S12). We will discuss the single-ion relaxation mechanism which can be correlated to experiments under very dilute conditions.

3.5 Single ion mechanism of magnetic relaxation

Ab initio CASSCF/RASSI-SO/SINGLE_ANISO calculation yields a moderate span 769.7(671.8) and 738.8(649.5) cm^{-1} of Dy1(Dy2) centre in **1** and **2**, respectively) of eight $^6H_{15/2}$ low-lying Kramers Doublets (KDs, Table S5–8) in **1** and **2**. The main magnetic axes of the two Dy centers in both complexes show obvious discrepancy (Fig. S12). In **1**, the main anisotropy axis of the Dy1 site is almost parallel to the O5-O8 direction, whereas for Dy2 it is tilted towards to the O9 atom. In **2**, the main magnetic axis of Dy1 and Dy2 sites are located parallel to the N2 and O10 atoms, respectively. However, the ground KD of **1** and **2** is found to possess a dominant contribution (≥ 95%) from m_J = |±15/2>, while the first excited KD is a hybrid state where the m_J = |±13/2> mixes with other states significantly (Figs. 5 and 6). The KD1-KD2 energy gap is estimated to be 235.2(189.1) and 211.5(212.3) cm^{-1} for the Dy1(Dy2) centre in **1** and **2,** respectively (Tables S5–8). The computed results reveal that the KD1-KD2 energy gap and crystal field splitting of the eight KDs are largest in the Dy1 centre of **1,** followed by the Dy1 centre of **2** (Table S5–8).

The computed *g* tensors (g_z = 19.648–19.788, $g_{x/y}$ = 0.002–0.030) imply an Ising ground state for both the complexes (Tables S5–8). This also suggests a very small QTM operative in the ground KD which is found to be in the range of 0.008–0.001 μ_B in the computed relaxation mechanism of complexes **1** and **2** (Figs. 5 and 6). While the TA-QTM in the KD2 of the Dy1 centre in **1** is found to be negligible (0.04 μ_B), the same is significant for the Dy2 centre (0.53 μ_B, Fig. 5(b)).

The g_{zz} axis of KD2 strongly deviates (12.2°) from the ground state for the Dy2 centre, reinforcing the magnetic relaxation via this state (Table S6). For the Dy1 centre of **1**, the magnetization relaxation occurs via the second excited state due to the significant TA-QTM process (0.37μ_B, Fig. 5(a)). This results in the U_{cal} value of 380.6 and 189.1 cm^{-1} for the Dy1 and Dy2 centre, respectively in **1**. For **2**, the magnetization relaxation occurs via first and second excited KD for Dy1 and Dy2 centre,

respectively, due to strong TA-QTM in the corresponding state, yielding an U_{cal} value of 337.9(212.3) cm^{-1} for Dy1(Dy2) centre of **2** (Tables S7 and 8, and Fig. 6). The computed single ion U_{cal} values are considerably higher than the estimated U_{cal} values in **1** and **2**, which suggest that the mechanism of relaxation is due to Dy_2 dimer and not based on single-ion anisotropy. Experimental studies indicate that complex **1** follows two relaxation paths with a blocking barrier of 75 and 33 cm^{-1}, while complex **2** display only one relaxation path with a blocking barrier of 23 cm^{-1}. This follows the single ion computed energy spectrum where the energy of KD2 and KD3 of the Dy1 and Dy2 metal centre is quite different in **1**; in contrast to complex **2** where the energy of KD2 is nearly identical in both metal centres (Tables S5–8).

We have also computed the crystal field parameter according to the Stevens Hamiltonian, $\widehat{H}_{CF} = \sum_{k=2,4,6} B_k^q \hat{O}_k^q$, where B_k^q and $\hat{O}_k^q$ correspond to the crystal field parameter and Stevens operator, respectively. The magnetic axiality of a complex is represented by the larger value of the axial crystal field parameter B_k^q $(k = 2,4,6;\ q = 0)$ compared to the non-axial crystal field parameter B_k^q $(k = 2,4,6, q \neq 0)$. The axial crystal field parameter B_2^0 is found to be larger for the Dy1 centre compared to the Dy2 in both complexes. This is in accordance with the crystal field splitting of the metal centre in **1** and **2**. The comparable values of B_2^0 and B_2^2 indicate small but significant operational QTM in the ground state for each metal centre in both complexes (Table S9).

3.6 Exchange coupled relaxation mechanism of complexes **1** and **2**

The experimental magnetic susceptibility was fitted using the POLY_ANISO module employing the Lines model.[52] Here, all the ab initio computed single ion anisotropic parameters were employed along with the total Dy(III)-Dy(III) exchange ($J_{Dy\text{-}Dy}$) using the Lines model.[52] The large intermolecular Dy···Dy distance *ca.* 1.2 nm implies that the intermolecular interaction can be neglected for both complexes. On the other hand, the shorter intramolecular distance indicates the exchange and dipolar interaction operative in **1** and **2**.

The experimental and computed magnetic susceptibility fitting yields a total $J_{Dy–Dy}$ of –0.21 and –0.17 cm^{-1} in **1** and **2**, respectively (Fig. 2). Furthermore, we have also computed the magnetic exchange in **1** and **2** with broken symmetry DFT calculations. The calculation yields an antiferromagnetic J of –0.09 and –0.08 cm^{-1} for **1** and **2**, respectively. These values agree well with the sign obtained from POLY_ANISO simulations, and the magnitudes are underestimated as only the exchange part was considered.

The average Dy–O–Dy angles for complexes **1** and **2** are 105.1° and 105.4° which falls in the region where antiferromagnetic coupling is expected with slightly larger angle yield slightly weaker antiferromagnetic coupling as shown in the earlier magneto-structural correlation developed for the Gd–O–Gd dimers.[53] The spin density plots are shown in Figs. S13 and S14, and the spin density of *ca.* 7.03 on Gd(III) suggests the mechanism of magnetic exchange occurs through spin polarization.

The antiferromagnetic exchange corroborates with the antiparallel alignment of the anisotropy axis of metal centres (Fig. S12). The tunnel splitting (Δ_{tun}) in the exchange-coupled ground (2.44×10^{-6} and

6.77×10^{-6} cm^{-1} for complexes **1** and **2,** respectively, Table S10 and 11) and first excited state is found to be very small, and it becomes significant in the second excited state (2.34×10^{-4} and 7.39×10^{-4} cm^{-1} for complexes **1** and **2**, respectively, Table S10 and 11), suggesting magnetization relaxation via this state. This results in the U_{cal} value of 189.2 and 211.6 cm^{-1} for exchange-coupled states in complexes **1** and **2**, respectively (Table S10 and S11, and Fig. S15). These exchange-coupled blocking barriers are also strongly overestimated compared to the experiments (75 and 33 cm^{-1} for **1** and 23 cm^{-1} for **2**). This has been noticed in several Dy_2 dinuclear complexes and this is essentially attributed to various factors such as QTM probability of the ground KD and other states, weaker exchange coupling that lead to faster tunneling etc. not being taken into consideration. Our earlier work by studying 31 different Dy_2 complexes proposed an equation which takes into consideration the above points. The proposed empirical Eq. (3) to estimate the

$$U_{\text{caleff}} = \left[\frac{U_{\text{cal1}}}{(\text{QTM/TA-QTM})\times 10^3} + \frac{U_{\text{cal2}}}{(\text{QTM/TA-QTM})\times 10^3}\right] + 15J \quad (3)$$

blocking barrier of Dy_2 complexes is shown,[54 - 56] where U_{cal1} and U_{cal2} indicate the single ion blocking barrier for Dy1 and Dy2 centre, respectively. The QTM/TA-QTM values correspond to the (x–1)th KD where magnetization relaxation occurs via xth KD. The magnetic exchange J is extracted from the fitting of temperature-dependent magnetic susceptibility using POLY_ANISO module. The U_{caleff} with equation (3) is estimated to be 37.2 and 31.1 cm^{-1} for complexes **1** and **2**, respectively. These values agree extremely well with the experimental estimates for **1** and **2** as well as reiterate the superiority of employing this equation to compute the effective energy barrier in Dy_2 dinuclear complexes.

4. Conclusions

Two dinuclear dysprosium coordination complexes were obtained by taking advantage of the mixed-ligand strategy consisting of oxazole derivative and Schiff-base. **1** and **2** were investigated by single-crystal X-ray diffraction, static and dynamic magnetic susceptibilities measurements as well as solid state fluorescence characterization. Single-crystal structure analyses provide the composition formulas information of **1** and **2** are $Dy_2(L_1)(L_2)(CH_3OH)_2{\cdot}CH_2Cl_2{\cdot}CH_3OH$ and $Dy_2(L_1)_2(L_3)_2(CH_3OH)_2{\cdot}CH_3CN$, respectively. Dynamic magnetic measurements reveal that **1** and **2** show frequency-dependent out-of-phase alternating-current susceptibility signal peaks at different temperatures under zero dc field, diagnostic of single-molecule magnet behavior. The experimental derived energy barrier to magnetization reversal for **1** and **2** are 108(1), 47(2) and 33(3) K. Ab initio CASSCF calculations were employed to disclose the reason behind the noticeable discrepancy of dynamic magnetization relaxation between **1** and **2**. Calculations reveal that intricate geometric differences lead to variation in single-ion anisotropy of the Dy(III) centres, and variation in the structural parameters such as Dy–O–Dy angles leads to different exchange coupling between **1** and **2**. We have shown that the effective energy barrier for Dy_2 systems can be estimated accurately based on the earlier equation proposed by us as other methods yield barrier heights that are orders of magnitude larger than the experimental estimates.

Solid state fluorescence measurements performed on **1** and **2** demonstrate that both exhibit two ligands centered components of fluorescent emissive, in addition, with different emitting colors and chromaticity coordinates. The discrepancy of fluorescence and single molecule magnet properties

showed by **1** and **2** can be attributed to the steric hindrance effect of Schiff base ligands. **1** and **2** are new members joined in the club of fluorescent single-molecule magnets bifunctional complexes. Our work demonstrates the initial attempt to evaluate the influence of steric hindrance of Schiff base ligand on dynamic magnetic properties and fluorescence of dinuclear dysprosium coordination complexes. Future work involving utilization of varied substituted groups such as fluorine, trifluoromethyl and cyano on Schiff-base or oxazole to affect the magnetic and fluorescence properties is underway in our lab.

Appendix A. Supplementary data

Supplementary data to this article can be found online at https://doi.org/101.1016/j.jre.

References

1. Huang Y, Li JX, Ge Y, Zhang XM, Xu Y, Li YH, et al. Designing asymmetric Dy_2 single-molecule magnets with two-step relaxation processes by the modification of the coordination environments of Dy(III) ions. *Dalton Trans. 2020*; *49(26)*: 8976.
2. Katoh K, Aizawa Y, Morita T, Breedlove BK, Yamashita M. Elucidation of dual magnetic relaxation processes in dinuclear dysprosium(III) phthalocyaninato triple-decker single-molecule magnets depending on the octacoordination geometry. *Chem Eur J. 2017*; *23(61)*: 15377.
3. Dolinar BS, Gómez-Coca S, Alexandropoulos DI, Dunbar KR. An air stable radical-bridged dysprosium single molecule magnet and its neutral counterpart: redox switching of magnetic relaxation dynamics. *Chem Commun. 2017*; *53(14)*: 2283.
4. Bera SP, Mondal A, Konar S. Investigation of the role of terminal ligands in magnetic relaxation in a series of dinuclear dysprosium complexes. *Inorg Chem Front. 2020*; *7(18)*: 3352.
5. Guettas D, Gendron F, Garcia GF, Riobé F, Roisnel T, Maury O, et al. Luminescence-driven electronic structure determination in a textbook dimeric Dy^{III}-based single-molecule magnet. *Chem Eur J. 2020*; *26(19)*: 4389.
6. Krylov DS, Schimmel S, Dubrovin V, Liu FP, Nguyen TTN, Spree L, et al. Substrate-independent magnetic bistability in monolayers of the single-molecule magnet $Dy_2ScN@C_{80}$ on metals and insulators. *Angew Chem Int Ed. 2020*; *59(14)*: 5756.
7. Wu HP, Li M, Xia ZQ, Montigaud V, Cador O, Guennic BL, et al. High temperature quantum tunneling of magnetization and thousand kelvin anisotropy barrier in a Dy_2 single-molecule magnet. *Chem Commun. 2021*; *57(3)*: 371.
8. Zhong L, Chen WB, Li XH, OuYang ZJ, Yang M, Zhang YQ, et al. Four dinuclear and one-dimensional-chain dysprosium and terbium complexes based on 2-hydroxy-3-methoxy benzoic acid: structures, fluorescence, single-molecule magnet, and ab initio investigation. *Inorg Chem. 2020*; *59(7)*: 4414.
9. Wang C, Sun R, Chen YF, Wang BW, Wang ZM, Gao S. Assembling high-temperature single-molecule magnets with low-coordinate bis(amido) dysprosium unit $[DyN_2]^+$ via Cl-K-Cl linkage. *CCS Chem*. 2020; *2(5)*: 362.
10. Yu S, Hu ZB, Chen ZL, Li B, Zhang YQ, Liang YN, et al. Two Dy(III) single-molecule magnets with their performance tuned by Schiff base ligands. *Inorg Chem. 2019*; *58(2)*: 1191.
11. Meng YS, Xiong J, Yang MW, Qiao YS, Zhong ZQ, Sun HL, et al. Experimental determination of magnetic anisotropy in exchange-bias dysprosium metallocene single-molecule magnets. *Angew Chem Int Ed. 2020*; *59(31)*: 13037.
12. Long J, Tolpygin AO, Cherkasov AV, Lyssenko KA, Guari Y, Larionova J, et al. Single-molecule magnet behavior in heterolopetic Dy^{3+}-chloro-diazabutadiene complexes: influence of the nuclearity and ligand redox state. *Dalton Trans*. *2020*; *49(34)*: 11890.
13. Han T, Giansiracusa MJ, Li ZH, Ding YS, Chilton NF, Winpenny REP, et al. Exchange-biasing in a dinuclear dysprosium(III) single-molecule magnet with a large energy barrier for magnetization reversal. *Chem Eur J. 2020*; *26(30)*: 6773.
14. Giansiracusa MJ, Al-Badran S, Kostopoulos AK, Whitehead GFS, McInnes EJL, Collison D, et al. Magnetic exchange interactions in symmetric lanthanide dimetallics. *Inorg Chem Front. 2020*; *7(20)*: 3909.

15. Huo Y, Chen YC, Wu SG, Liu JL, Jia JH, Chen WB, et al. Effect of bridging ligands on magnetic behavior in dinuclear Dy cores supported by polyoxometalates. *Inorg Chem. 2019*; *58(2)*: 1301.
16. Horii Y, Katoh K, Sugimoto K, Nakanishi R, Breedlove BK, Yamashita M. Detailed analysis of the crystal structures and magnetic properties of a Dy(III) phthalocyaninato sextuple-decker complex: weak f-f interactions suppress magnetic relaxation. *Chem Eur J. 2019*; *25(12)*: 3098.
17. Peng Y, Mereacre V, Baniodeh A, Lan YH, Schlageter M, Kostakis GE, et al. Effect of ligand field tuning on the SMM behavior for three related alkoxide-bridged dysprosium dimers. *Inorg Chem. 2016*; *55(1)*: 68.
18. Shen FX, Pramanik K, Brandão P, Zhang YQ, Jana NC, Wang XY, et al. Macrocycle supported dimetallic lanthanide complexes with slow magnetic relaxation in Dy_2 analogues. *Dalton Trans*. *2020*; *49(40)*: 14169.
19. Mikhalyova EA, Zeller M, Jasinski JP, Butcher RJ, Carrella LM, Sedykh AE, et al. Combination of single-molecule magnet behavior and luminescence properties in a new series of lanthanide complexes with tris(pyrazolyl) borate and oligo(β-diketonate) ligands. *Dalton Trans*. *2020*; *49(23)*: 7774.
20. Pointillart F, Ou-Yang JK, Garcia GF, Montigaud V, Gonzalez JF, Marchal R, et al. Tetrathiafulvalene-based helicene ligand in the design of a dysprosium field-induced single-molecule magnet. *Inorg Chem. 2019*; *58(1)*: 52.
21. Bernot K, Daiguebonne C, Calvez G, Suffren Y, Guillou O. A journey in lanthanide coordination chemistry: from evaporable dimers to magnetic materials and luminescent devices. *Acc Chem Res. 2021*; *54(2)*: 427.
22. Díaz-Ortega IF, Herrera JM, Aravena D, Ruiz E, Gupta T, Rajaraman G, et al. Designing a Dy_2 single-molecule magnet with two well-differentiated relaxation processes by using a non symmetric bis-bidentate bipyrimidine-N-oxide ligand: a comparison with mononuclear counterparts. *Inorg Chem. 2018*; *57(11)*: 6362.
23. Zhang WY, Tian YM, Li HF, Chen P, Sun WB, Zhang YQ, et al. A series of dinuclear Dy(III) complexes bridged by 2-methyl-8-hydroxylquinoline: replacement on the periphery coordinated β-diketonate terminal leads to different single-molecule magnetic properties. *Dalton Trans*. *2016*; *45(9)*: 3863.
24. Vignesh KR, Alexandropoulos DI, Dolinar BS, Dunbar KR. Hard versus soft: zero-field dinuclear Dy(III) oxygen bridged SMM and theoretical predictions of the sulfur and selenium analogues. *Dalton Trans*. *2019*; *48(9)*: 2872.
25. Lemes MA, Mavragani N, Richardson P, Zhang YX, Gabidullin B, Brusso JL, et al. Unprecedented intramolecular pancake bonding in a $\{Dy_2\}$ single-molecule magnet. *Inorg Chem Front. 2020*; *7(14)*: 2592.
26. Mattei CA, Montigaud V, Gendron F, Denis-Quanquin S, Dorcet V, Giraud N, et al. Solid-state versus solution investigation of a luminescent chiral BINOL-derived bisphosphate single-molecule magnet. *Inorg Chem Front. 2021*; *8(4)*: 947.
27. Hahn P, Ullmann S, Klose J, Peng Y, Powell AK, Kersting B. Dinuclear Tb and Dy complexes supported by hybrid Schiff-base/calixarene ligands: synthesis, structures and magnetic properties. *Dalton Trans*. *2020*; *49(31)*: 10901.
28. Liu JC, Huang XD, Zou Q, Bao SS, Wang XZ, Ma JY, et al. Synergetic magnetic and luminescence switching via solid state phase transitions of the dysprosium−dianthracene complex. *J Mater Chem C*.

2020; *8(22)*: 7369.
29. Gao F, Feng XW, Yang L, Chen XY. New sandwich-type lanthanide complexes based on closed-macrocyclic Schiff base and phthalocyanine molecules. *Dalton Trans*. *2016*; *45(17)*: 7476.
30. Zhang P, Perfetti M, Kern M, Hallmen PP, Ungur L, Lenz S, et al. Exchange coupling and single molecule magnetism in redox-active tetraoxolene-bridged dilanthanide complexes. *Chem Sci. 2018*; *9(5)*: 1221.
31. Gould CA, Mu E, Vieru V, Darago LE, Chakarawet K, Gonzalez MI, et al. Substituent effects on exchange coupling and magnetic relaxation in 2,2'-bipyrimidine radical-bridged dilanthanide complexes. *J Am Chem Soc. 2020*; *142(50)*: 21197.
32. Wang HL, Qian K, Qi DD, Cao W, Wang K, Gao S, et al. Co-crystallized fullerene and a mixed (phthalocyaninato)(porphyrinato) dysprosium double-decker SMM. *Chem Sci. 2014*; *5(8)*: 3214.33.
33. Ke HS, Yang YS, Wei W, Jiang YD, Zhang YQ, Xie G, et al. Synergistic effect of mixed ligands on the anisotropy axis of two dinuclear dysprosium complexes. *Dalton Trans*. *2020*; *49(30)*: 10594.
34. Alexandropoulos DI, Fournet A, Cunha-Silva L, Mowson AM, Bekiari V, Christou G, et al. Fluorescent naphthalene diols as bridging ligands in Ln^{III} cluster chemistry: synthetic, structural, magnetic, and photophysical characterization of Ln^{III}_8 "christmas stars". *Inorg Chem. 2014*; *53(11)*: 5420.
35. Manzur J, Santana RC, Maia LJQ, Vega A, Spodine E. Tuning white light emission in dinuclear phenoxo bridged Dy^{III} complexes. *Inorg Chem. 2019*; *58(15)*: 10012.
36. Xie SF, Huang LQ, Zhong L, Lai BL, Yang M, Chen WB, et al. Structures, single-molecule magnets, and fluorescent properties of four dinuclear lanthanide complexes based on 4-azotriazolyl-3-hydroxy-2-naphthoic acid. *Inorg Chem. 2019*; *58(9)*: 5914.
37. Liu MJ, Wu SQ, Li JX, Zhang YQ, Sato O, Kou HZ. Structural modulation of fluorescent rhodamine-based dysprosium(III) single-molecule magnets. *Inorg Chem. 2020*; *59(4)*: 2308.
38. Guo PH, Meng Y, Chen YC, Li QW, Wang BY, Leng JD, et al. A zigzag Dy^{III}_4 cluster exhibiting single-molecule magnet, ferroelectric and white-light emitting properties. *J Mater Chem C*. *2014*; *2(42)*: 8858.
39. Anastasiadis NC, Kalofolias DA, Philippidis A, Tzani S, Raptopoulou CP, Psycharis V, et al. A family of dinuclear lanthanide(III) complexes from the use of a tridentate Schiff base. *Dalton Trans*. *2015*; *44(22)*: 10200.
40. Wang HL, Ma XF, Zou HH, Wang K, Li B, Chen ZL, et al. Mixed chelating ligands used to regulate the luminescence of Ln(III) complexes and single-ion magnet behavior in Dy-based analogues. *Dalton Trans. 2018*; *47(44)*: 15929.
41. Cao DK, Gu YW, Feng JQ, Cai ZS, Ward MD. Mononuclear lanthanide complexes incorporating an anthracene group: structural modification, slow magnetic relaxation and multicomponent fluorescence emissions in Dy compounds. *Dalton Trans*. *2013*; *42(32)*: 11436.
42. Liu CM, Zhang DQ, Zhang YQ, Li M, Zhu DB. Both magnetic relaxation and luminescence of Zn_2Dy_2 cluster complexes regulated by the bis-imine chain in Schiff base ligands. *New J Chem. 2019; 43(36)*: 14502.
43. Vicente R, Tubau À, Speed S, Mautner FA, Bierbaumer F, Fischer RC, et al. Slow magnetic relaxation and luminescence properties in neodymium(III)-4,4,4-trifluoro-1-(2-naphthyl)butane-1,3-dionato complexes incorporating bipyridyl ligands. *New J Chem. 2021; 45(32)*: 14713.

44. Rufino-Felipe E, Caballero-Jiménez J, Guerrero-Ramírez LG, Flores-Álamo M, Muñoz-Hernández MÁ. Novel hexanuclear and octanuclear zinc alkyl cages derived from a bis-oxamidate ligand. *Inorg Chem Commun. 2016*; *63*: 107.
45. Khomenko TM, Salomatina OV, Kurbakova SY, Il'ina IV, Volcho KP, Komarova NI, et al. New chiral ligands from myrtenal and caryophyllene for asymmetric oxydation of sulfides catalyzed by metal complexes. *Russian J Organic Chem*. *2006*; *42(11)*: 1653.
46. Sheldrick GM. SHELXT-Integrated space-group and crystal-structure determination. *Acta Crystallograph Sec A. 2015*; *71(1)*: 3.
47. Casanova D, Llunell M, Alemany P, Alvarez S. The rich stereochemistry of eight-vertex polyhedra: A continuous shape measures study. *Chem Eur J. 2005*; *11(5)*: 1479.
48. Guo YN, Xu GF, Guo Y, Tang JK. Relaxation dynamics of dysprosium(III) single molecule magnets. *Dalton Trans. 2011*; *40(39)*: 9953.
49. Aubin SMJ, Sun ZM, Pardi L, Krzystek J, Folting K, Brunel LC, et al. Reduced anionic Mn_{12} molecules with half-integer ground states as single-molecule magnets. *Inorg Chem. 1999*; *38(23)*: 5329.
50. Zhang L, Liu J, Gao JK, Lu R, Liu F. Adjustment of the solid fluorescence of a chalcone derivative through controlling steric hindrance. *RSC Adv. 2017*; *7(73)*: 46354.
51. Kumar P, Biswas S, Swain A, Acharya J, Kumar V, Kalita P, et al. Azide-coordination in homometallic dinuclear lanthanide(III) complexes containing nonequivalent lanthanide metal ions: zero-field SMM behavior in the dysprosium analogue. *Inorg Chem. 2021*; *60(12)*: 8530.
52. Lines ME. Orbital angular momentum in the theory of paramagnetic clusters. *J Chem Phys. 1971*; *55(6)*: 2977.
53. Rajeshkumar T, Singh SK, Rajaraman G. A computational perspective on magnetic coupling, magneto-structural correlations and magnetic-caloric effect of a ferrromagnetically coupled $\{Gd^{III}$-$Gd^{III}\}$ pair. *Polyhedron. 2013*; *52*: 1299.
54. Dey S, Rajaraman G. An approach to estimate the barrier height for magnetization reversal in $\{Dy_2\}$ SMMs using ab initio calculations. *Dalton Trans*. *2020*; *49(42)*: 14781.
55. Ding YS, Zheng YZ. Anisotropic magnetocaloric effect in a dysprosium(III) single-molecule magnet − Commemorating the 100th anniversary of the birth of Academician Guangxian Xu. *J. Rare Earths*. *2021, 39*: 1554.
56. Xu CY, Wu ZL, Fan CJ, Yan LL, Wang WM, Ji BM. Synthesis of two lanthanide clusters Ln^{III}_4 (Gd_4 and Dy_4) with [2 × 2] square grid shape: magnetocaloric effect and slow magnetic relaxation behaviors. *J. Rare Earths*. *2021, 39*: 1082.

Figure captions:

Fig. 1 Molecular structure**s** of **1** (a) and **2** (b). Hydrogen atoms and dissociative solvent molecules are omitted for clarity. Color code: Dy (yellow), C (black and pink), N (blue) and O (red). The turquoise lines highlight the deprotonated form of ligand L_1 and its coordinated atoms to dysprosium ions; the green lines mark both L_2 (a) and L_3 (b). Methyl groups of each tert-butyl part are removed and the remaining carbon atoms are depicted as pink balls.

Fig. 2 Temperature dependence of $\chi_M T$ measured on powder samples of **1** (a) and **2** (b) under 0.1 T dc applied field. The red solid line corresponds to the fitted $\chi_M T$ from POLY_ANISO calculation. As the computed magnetic susceptibility was underestimated compared to the experiment, a scaling factor of 1.01 was used during the fitting.

Fig. 3 The frequency dependent out-of-phase magnetic susceptibility components for **1** (a) and **2** (b) under zero direct-current field. Solid lines represent best fitting with equation.

Fig. 4 Plot of $\ln\tau$ versus inverse temperature for **1** (a) and **2** (b). Red solid lines represent Arrhenius linear fitting and green solid lines correspond to multiple relaxation processes fitting as dictated in the text.

Fig. 5 The mechanism of magnetization relaxation of Dy1 (a) and Dy2 (b) centres in **1**. The red arrow corresponds to the QTM/TA-QTM via ground/excited KD. The sky dotted arrow corresponds to the Orbach process. The green arrow corresponds to the most possible pathway for magnetization relaxation. The blue characters indicate the m_J composition of a KD.

Fig. 6 The mechanism of magnetization relaxation of Dy1 (a) and Dy2 (b) centres of **2**. See Fig. 5 for color description

Graphical abstract:

We demonstrate the steric hindrance effect of Schiff base ligands on magnetic relaxation dynamics and emissive behavior of two dinuclear dysprosium complexes.

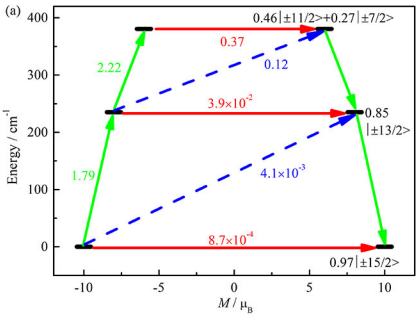

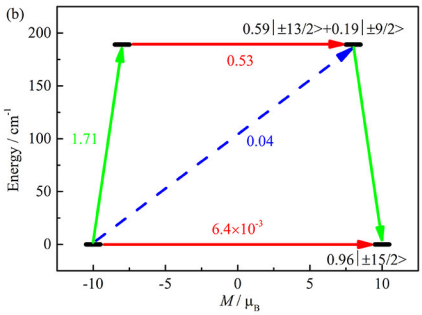

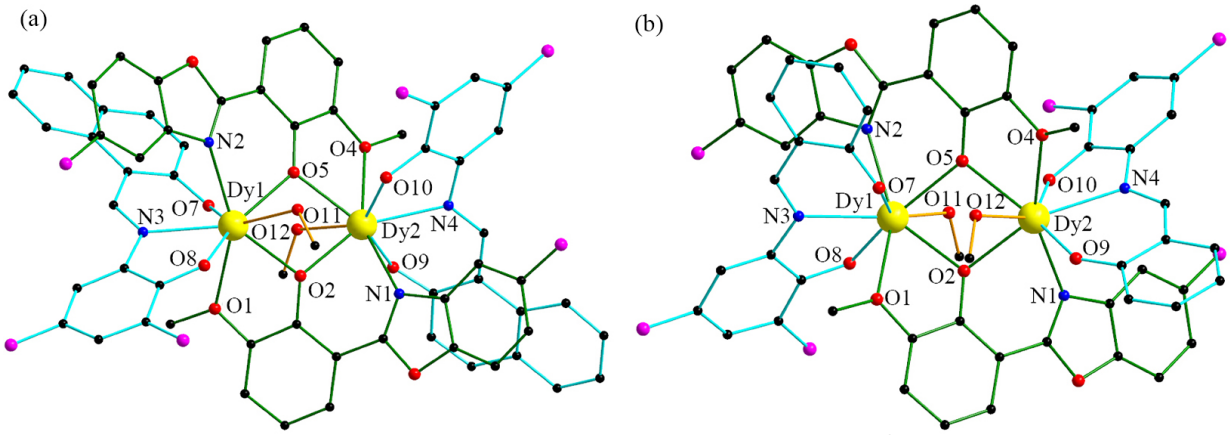

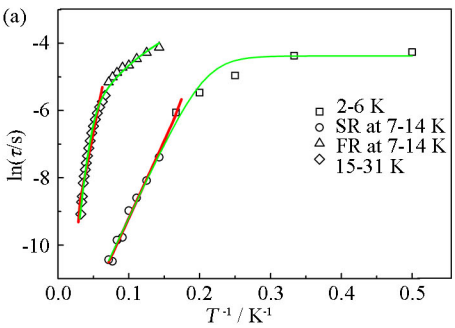

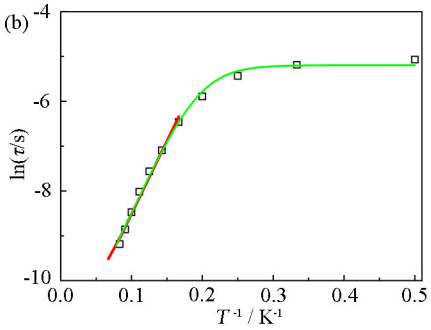

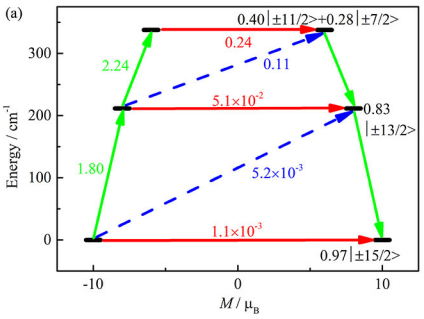

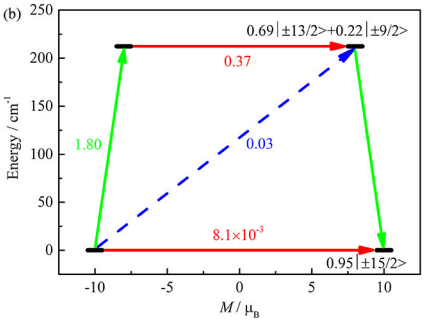

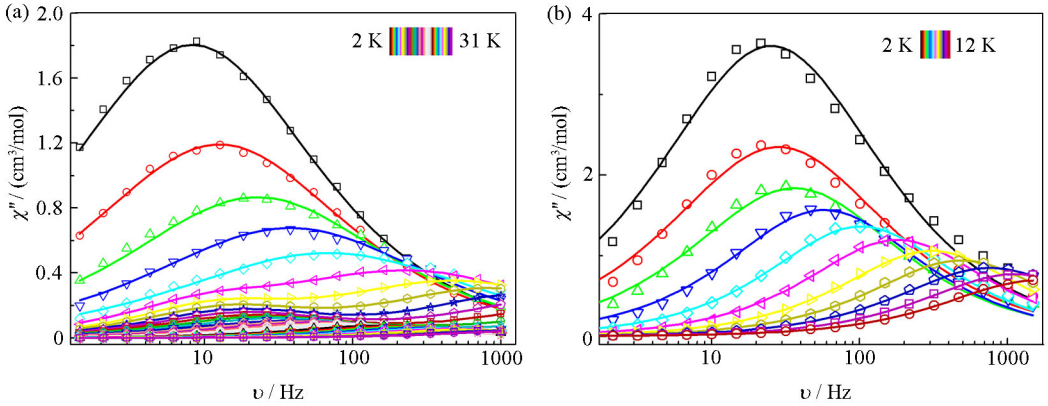

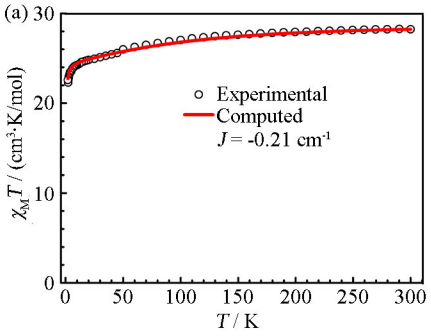

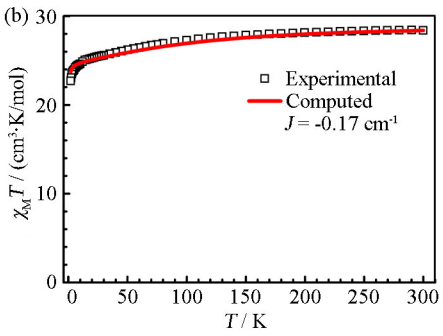

Dear Editor,

We declare that no conflict of interest exits in the submission of this manuscript, and the manuscript is approved by all authors for publication. I would like to declare on behalf of my co-authors that the work described is an original research that has not been published previously, and not under consideration for publication elsewhere, in whole or in part. All the authors listed have approved the enclosed manuscript.

Corresponding author:

Dr. Hongshan Ke

College of Chemistry and Materials Science

Northwest University

Xi'an 710069, P. R. China

E-mail: hske@nwu.edu.cn